Supplement of Atmos. Chem. Phys., 26, 1967–1992, 2026
https://doi.org/10.5194/acp-26-1967-2026-supplement
© Author(s) 2026. CC BY 4.0 License.

Atmospheric Chemistry and Physics
Open Access
EGU

Supplement of

Modelling the impact of anthropogenic aerosols on CCN concentrations over a rural boreal forest environment

Petri Clusius et al.

Correspondence to: Petri Clusius (petri.clusius@helsinki.fi)

The copyright of individual parts of the supplement might differ from the article licence.

Dry deposition of particles

The average deposition velocities over land and sea (with land-sea mask cut-off as 0.8 for land and 0.2 for sea) are shown in Fig 3, which also shows settling velocities from studies reported in Farmer et al. (2021) for forest land (Höfken and Gravenhorst, 1982; Grosch and Schmitt, 1988; Lorenz and Murphy, 1989; Waraghai and Gravenhorst, 1989; Gallagher et al., 1997; Gaman et al., 2004; Pryor, 2006; Grönholm et al., 2007; Pryor et al., 2008; Groenholm et al., 2009; Pryor et al., 2009; Vong et al., 2010; Gordon et al., 2011; Mammarella et al., 2011; Lavi et al., 2013; Zhang et al., 2014) and for water surfaces (Möller and Schumann, 1970; Sehmel, 1973; Caffrey et al., 1998; Zufall et al., 1998; Qi et al., 2020). The rates in the model followed the same general profile with observations, where the minimum was around 0.2 cm m^{-1} at 100 nm over land and 0.03 cm m^{-1} at 200 nm over sea.

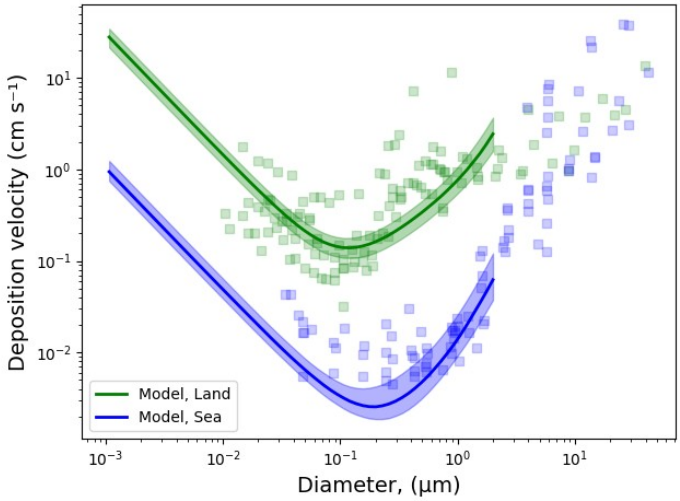

Figure S1: Median dry deposition velocities of aerosols in SOSAA over land (land-sea mask>0.8, green) and sea (land-sea mask<0.2, blue), with shaded interquartiles. The square markers are from Farmer et al. (2021), showing combined results from 16 (forest) and 5 (sea) studies.

SOSAA PreProcessor (SPP)

For a given gas compound or primary aerosol particle we get the average emissions $\langle E_\sigma \rangle$ from a given sector σ at time t with

$$\langle E_{t,\sigma} \rangle = \frac{E_{\sigma,t,k,j} SRR_{t,k,j}}{\sum_{k,j} SRR_{t,k,j}} \quad (1)$$

where *t*, *k* and *j* are the time, and latitude and longitude grid indices, respectively. The mean emission E is a representation of the average emissions affecting the airmasses at that time. The CAMS emissions are provided as mean of different timescales and amended with temporal profiles (diurnal and/or weekly), which are applied by SPP based on

the emission source sectors, times and locations of the SRR weight factors. Anthropogenic emissions also have a vertical profile, and here we followed the method in EMEP MSC-W chemical transport model (Simpson et al., 2012) and used a spatio-temporally constant but sector dependent 12-layer profile for all emissions from CAMS-ANT and GAINS particles, extending from 0 to 900 metres above the ground. In this study we summed all the sector specific emissions before using it as input in SOSAA, therefore following Eq. 1 the final emissions for a given compound along a trajectory is obtained by

$$\langle E_t \rangle = \sum_{\sigma} V_{\sigma} \langle E_{t,\sigma} \rangle \quad (2)$$

where V_σ is the vertical profile for sector σ. The output of SPP is a NetCDF file with emission rates (in kg m^{-2} s^{-1}) of the processed compounds as trajectories, separate for each emission dataset. The names of the emitted gaseous compounds in CAMS and their counterpart in the chemistry scheme are shown in Table S1.

Table S1: CAMS global emission variables and the compounds they were associated in SOSAA chemistry. Note the SO_2 emission reduction factor 0.5. Data sources: A= GAMS-GLOB-ANT, B= GAMS-GLOB-BIO.

Name in CAMS datasets	MCM long name	in chemistry	Source in CAMS	Fraction (mass)
hexanes	HEXANE (N-HEXANE)	NC6H14	A	
butanes	N-BUTANE	NC4H10	A	
pentanes	PENTANE (N-PENTANE)	NC5H12	A	
propane	PROPANE	C3H8	A	
other-VOCs	Not used	Not used	A	
ethane	ETHANE	C2H6	A	
benzene	BENZENE	BENZENE	A	
ethene	ETHENE (ETHYLENE)	C2H4	A	
xylene	1,2-DIMETHYL BENZENE (O-XYLENE)	OXYL	A	0.33
-:-	1,3-DIMETHYL BENZENE (M-XYLENE)	MXYL	A	0.33
-:-	1,4-DIMETHYL BENZENE (P-XYLENE)	PXYL	A	0.33
alcohols	METHANOL	CH3OH	A	0.2
-:-	ETHANOL	C2H5OH	A	0.2
-:-	1-PROPANOL (N-PROPANOL)	NPROPOL	A	0.3
-:-	2-PROPANOL (I-PROPANOL)	IPROPOL	A	0.3
other-alkanes-and-alkynes	Not used	Not used	A	
other-aromatics	ETHENYL BENZENE (STYRENE)	STYRENE	A	
toluene	METHYLBENZENE (TOLUENE)	TOLUENE	A	
other-aldehydes	ETHANAL (ACETALDEHYDE)	CH3CHO	A	
acetylene	ETHYNE (ACETYLENE)	C2H2	A	
propene	PROPENE (PROPYLENE)	C3H6	A	
formaldehyde	METHANAL (FORMALDEHYDE)	HCHO	A	
trimethylbenzene	1,2,3-TRIMETHYL BENZENE (HEMIMELLITENE)	TM123B	A	0.33
-:-	1,2,4-TRIMETHYL BENZENE (PSEUDOCUMENE)	TM124B	A	0.33
-:-	1,3,5-TRIMETHYL BENZENE (MESITYLENE)	TM135B	A	0.33
total-ketones	PROPANONE (ACETONE)	CH3COCH3	A	
esters	METHYL FORMATE	CH3OCHO	A	
ethers	DIMETHYL ETHER	CH3OCH3	A	
total-acids	METHANOIC ACID	HCOOH	A	
monoterpenes	ALPHA-PINENE	APINENE	A	0.38
-:-	BETA-PINENE	BPINENE	A	0.27
-:-	LIMONENE	LIMONENE	A	0.09
-:-	-	CARENE	A	0.17
-:-	-	SABINENE	A	0.1
isoprene	2-METHYL-1,3-BUTADIENE (ISOPRENE)	C5H8	A	
methanol	METHANOL	CH3OH	B	
other-monoterpenes	LIMONENE	LIMONENE	B	0.25
-:-	-	CARENE	B	0.48
-:-	-	SABINENE	B	0.28
acetone	PROPANONE (ACETONE)	CH3COCH3	B	
pinene-a	ALPHA-PINENE	APINENE	B	
pinene-b	BETA-PINENE	BPINENE	B	
isoprene	2-METHYL-1,3-BUTADIENE (ISOPRENE)	C5H8	B	
ethene	ETHENE (ETHYLENE)	C2H4	B	
propene	PROPENE (PROPYLENE)	C3H6	B	
ethanol	ETHANOL	C2H5OH	B	
acetaldehyde	ETHANAL (ACETALDEHYDE)	CH3CHO	B	

sesquiterpenes	BETA-CARYOPHYLLENE	BCARY	B	
butenes-and-higher-alkenes	1-BUTENE	BUT1ENE	B	0.5
-:-	1-PENTENE	PENT1ENE	B	0.3
-:-	1-HEXENE	HEX1ENE	B	0.2
formaldehyde	METHANAL (FORMALDEHYDE)	HCHO	B	
other-aldehydes	ETHANAL (ACETALDEHYDE)	CH3CHO	B	0.7
-:-	PROPANAL (PROPRIONALDEHYDE)	C2H5CHO	B	0.3
toluene	METHYLBENZENE (TOLUENE)	TOLUENE	B	
other-ketones	BUTANONE (METHYL ETHYL KETONE)	MEK	B	
MBO	2-METHYL-3-BUTEN-2-OL	MBO	B	
hydrogen-cyanide	-	-	B	
methyl-choride	CHLOROMETHANE (METHYL CHLORIDE)	CH3CL	B	
ethane	ETHANE	C2H6	B	
methyl-bromide	BROMOMETHANE	CH3BR	B	
methyl-iodide	-	CH3I	B	
propane	PROPANE	C3H8	B	
Butanes-and-higher-alkanes	N-BUTANE	NC4H10	B	
CH_4	METHANE	CH4	B	
DMS	DIMETHYL SULPHIDE	DMS	B	
CO	CO	CO	B	
CH_4	METHANE	CH4	A	
SO_2	SO2	SO2	A	0.5
NH_3	No chemical reactions; only used in clustering with H_2SO_4	NH3	A	
NO_X	NO	NO	A	0.2
-:-	NO2	NO2	A	0.8
CO	CO	CO	A	

Kappa parameters for CCN

Table S2: κ values used to calculate CCN concentration. Range estimation was done by adding the upper or lower limits (shown in parenthesis) to nominal κ. The upper and lower range were chosen from the spread in κ estimations in literature, (references in "Comment").

Composition	κ_c	*Comment*
Primary particles	*0.208 (-0.1, +0.2)*	*levoglucosan (kappa=0.208) (*Petters and Kreidenweis, 2007)
Secondary organics	*0.15 (-0.1,+0.1)*	*Adapted from* Paramonov et al. (2013) *, who report values between 0.1 and 0.2 for high organic fractions.*
Sea salt	*1.28 (-0.1,+0.2)*	*(Petters and Kreidenweis, 2007). This value has been shown to be too small (*Paramonov et al., 2013)
Sulfuric acid	*1.0 (-0.2,+0.2)*	*J. Schmale et al., ideal case*
Molecular clusters	*0.9 (-0.3,0)*	*Ammonium bisulfate (*Petters and Kreidenweis, 2007)

Statistical descriptors

Normalized Mean Bias Factor (B_{NMBF}, Yu et al., 2006):

$$B_{NMBF} = \begin{cases} \frac{\sum_i M_i}{\sum_i O_i} - 1, \text{ when } \bar{M} \geq \bar{O} \\ 1 - \frac{\sum_i O_i}{\sum_i M_i}, \text{ when } \bar{M} < \bar{O} \end{cases}, B_{NMBF} = [-\infty, \infty] \quad (3)$$

Mean Factor Bias and Mean Factor Error (EPA, 2007):

$$MFB = \frac{2}{N} \frac{\sum_N (M_i - O_i)}{\sum_N M_i + O_i} \times 100\%, [-200\%, 200\%] \quad (4)$$

$$MFE = \frac{2}{N} \frac{\sum_N |M_i - O_i|}{\sum_N M_i + O_i}, [0, \infty] \quad (5)$$

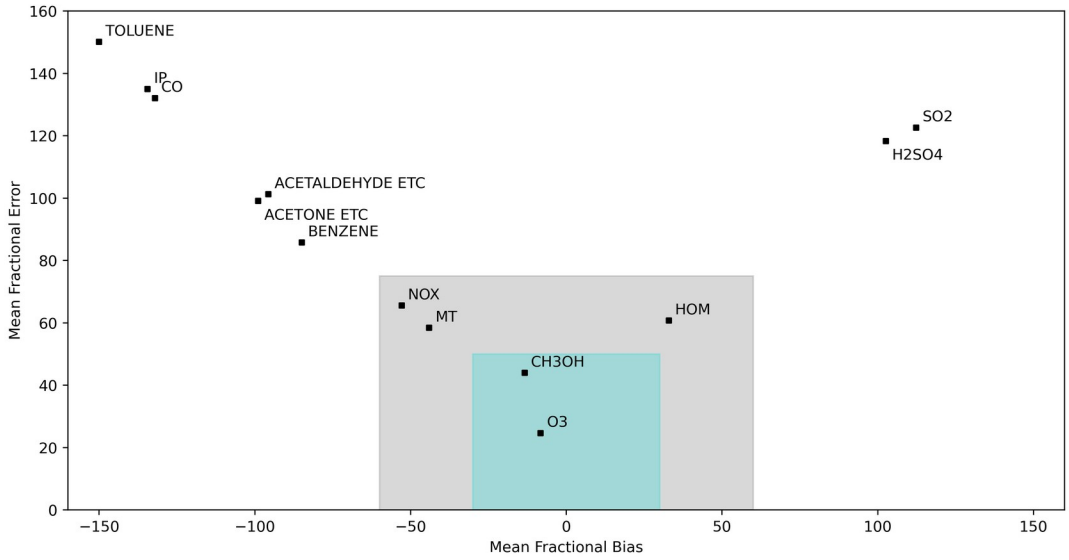

Figure S2: Daily median MFB and MFE in an EPA model evaluation criteria field.

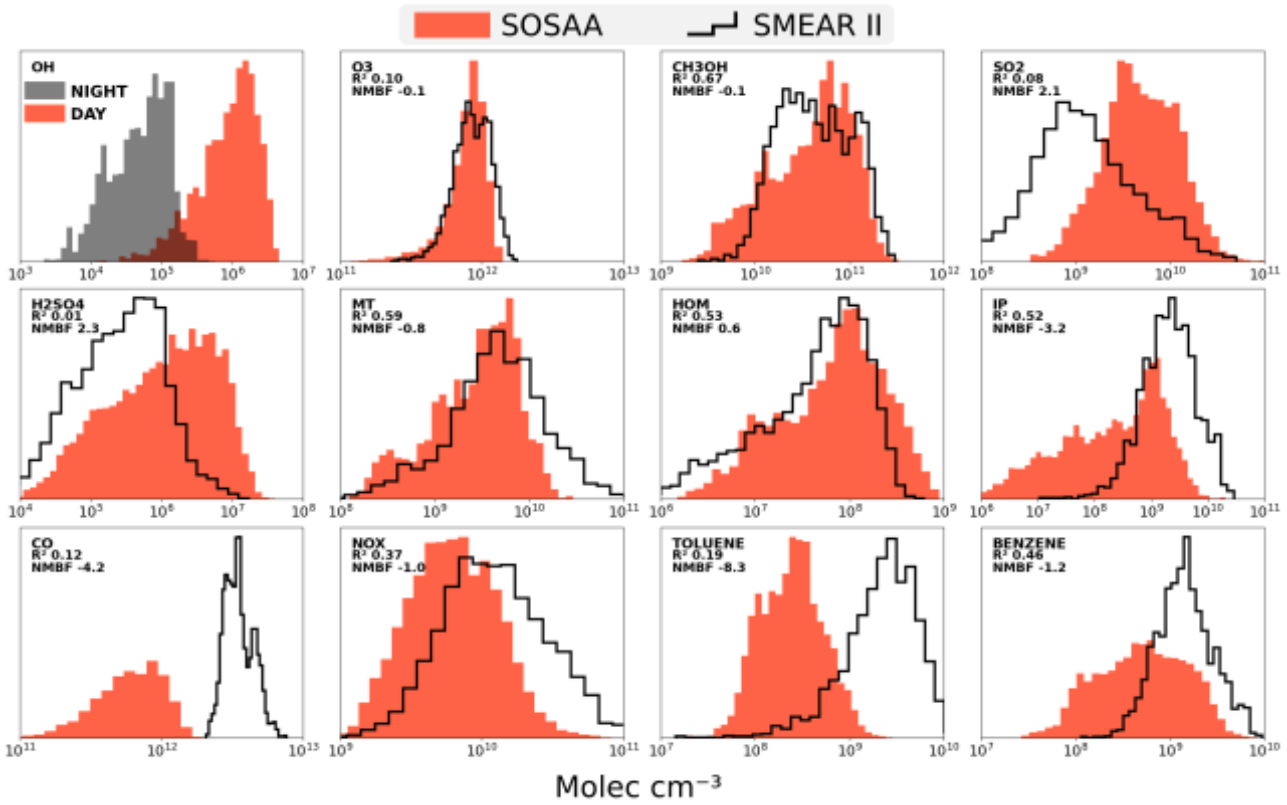

Figure S3: Distributions of gas concentrations during Mar-Oct 2018 in SOSAA model and SMEAR II measurements.

Modelled CCN number concentrations, critical diameters and κ

Table S3: Mean CCN number concentration, critical dry diameter D_{crit}, κ at D_{crit} and mean κ of CCN>D_{crit} for the modelled supersaturation classes. Figures in parentheses show the minimums and maximums calculated using the range of κ shown in Table S2.

Supersaturation	NC (cm^{-3})	Critical dry diameter (nm)	Critical κ	Mean κ
0.1 %	193 (171–225)	176.0 (155.7–193.0)	0.330 (0.258–0.468)	0.275 (0.232–0.370)
0.2 %	339 (315–374)	111.3 (99.6–120.9)	0.328 (0.263–0.450)	0.255 (0.208–0.352)
0.4 %	512 (488–546)	70.2 (63.7–75.3)	0.329 (0.274–0.433)	0.246 (0.198–0.342)
0.6 %	629 (607–661)	53.6 (49.1–57.0)	0.331 (0.282–0.424)	0.243 (0.195–0.338)
0.8 %	720 (700–750)	44.3 (40.8–46.9)	0.332 (0.287–0.417)	0.241 (0.193–0.336)
1.0 %	796 (772–824)	38.2 (35.3–40.3)	0.332 (0.290–0.412)	0.240 (0.192–0.334)
1.2 %	861 (835–888)	33.9 (31.4–35.7)	0.331 (0.292–0.408)	0.239 (0.192–0.333)

Impact of H_2SO_4, NH_3 CS and Temperature in cluster formation rates from ACDC

Figure S7 shows the averaged changes in cluster formation rates along the trajectories in the ZeroPNE compared to BASE. As the coagulation sink generally decreased, the effect was on average approximately threefold increase in new particle formation. Notably, at time periods when the model and observations showed low concentrations in the nucleation modes (July and early September), ZeroPNE showed up to tenfold increase in cluster formation rates, indicating that the primary emissions were heavily suppressing the cluster formation in those time periods.

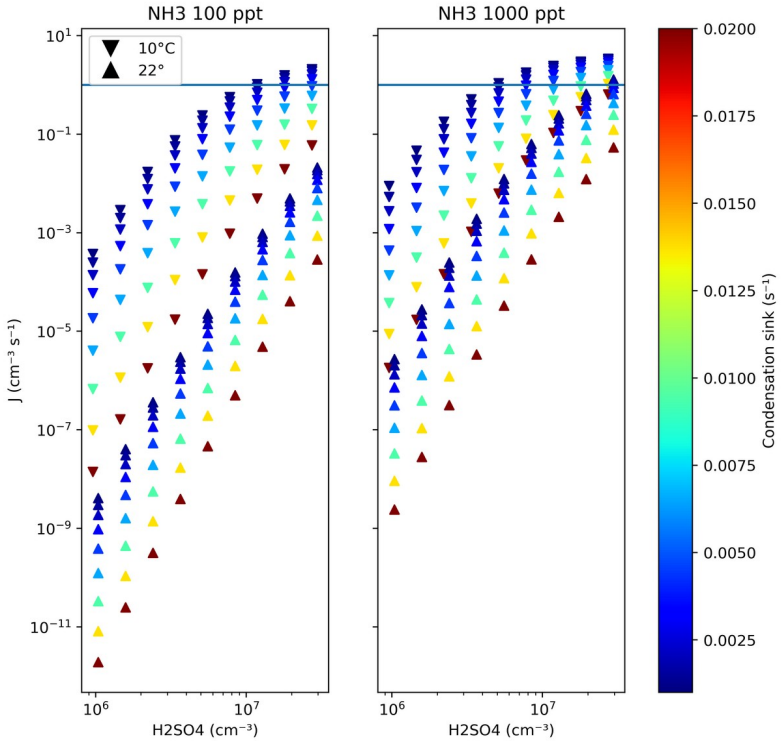

Figure S4: Sensitivity of the H_2SO_4–NH_3 chemistry in ACDC to key parameters: monomer concentrations, condensation sink (which is used to scale the coagulation sink of the interstitial clusters) and temperature. These values are from steady state simulations. The blue line marks 1 cm^{-3} s^{-1}.

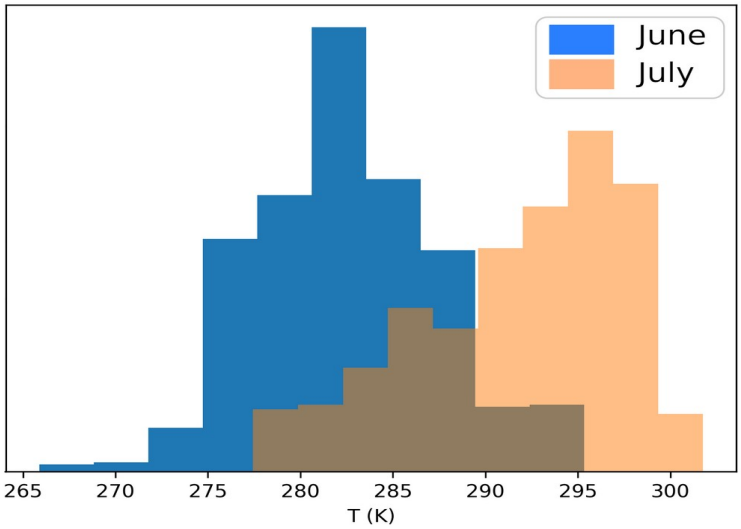

Figure S5: Mean 8 am temperatures along the trajectory between 0–96 hours.

Figures 4 and 5 show the effect of condensation sink and temperature to formation rate as function of monomer concentations. The temperatures (10°C and 22°C) were selected to represent the mode of the temperatures at 8 am (UTC, these are not necessarily local times) along the trajectories in June (10°C) and July (12°). Even at 1 ppb ammonia and 3×10^7 H_2SO_4 concentrations, at 22°C and high condensation sink, the nucleation rates fall well below 1 cm^{-3} s^{-1}.

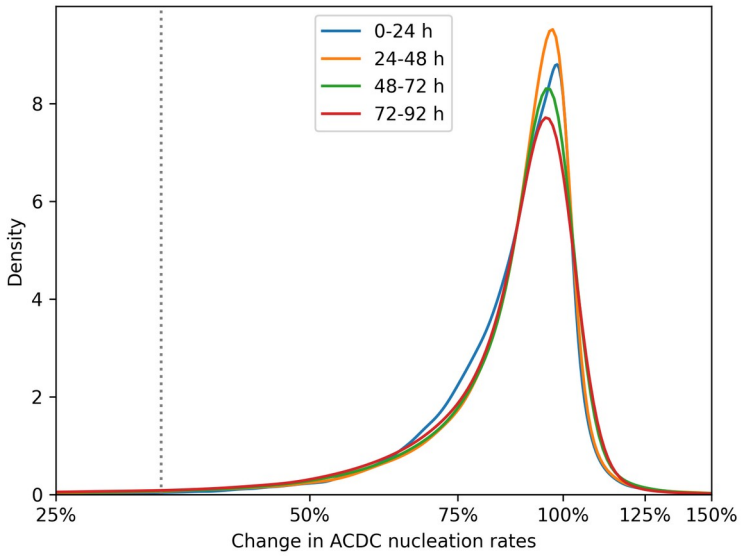

Figure S6: Change in ACDC nucleation module due to multiplying the cluster formation rates outside ACDC by a factor of 3. The dashed vertical line shows approximately 33% limit, where the multiplication factor is being offset by decrease in ACDC due to increased condensation sink. The mean value of these distributions (0.873) was used to correct the f_I in the response analysis (leading to f_I=2.62).

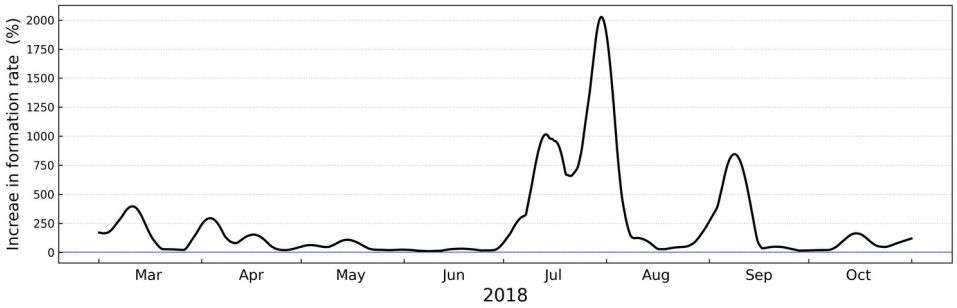

Figure S7: 12 day running mean of the enhancement of nucleation rates calculated by ACDC when primary particle emissions were turned off. The data was calculated from the ratio of the mean nucleation rates for the last 96 hours along the trajectory for ZeroPNE and BASE, then a running mean smoothing was applied. The largest increases in nucleation rates coincide with the peaks in the response of modelled CCN 1.0% to the primary particles.

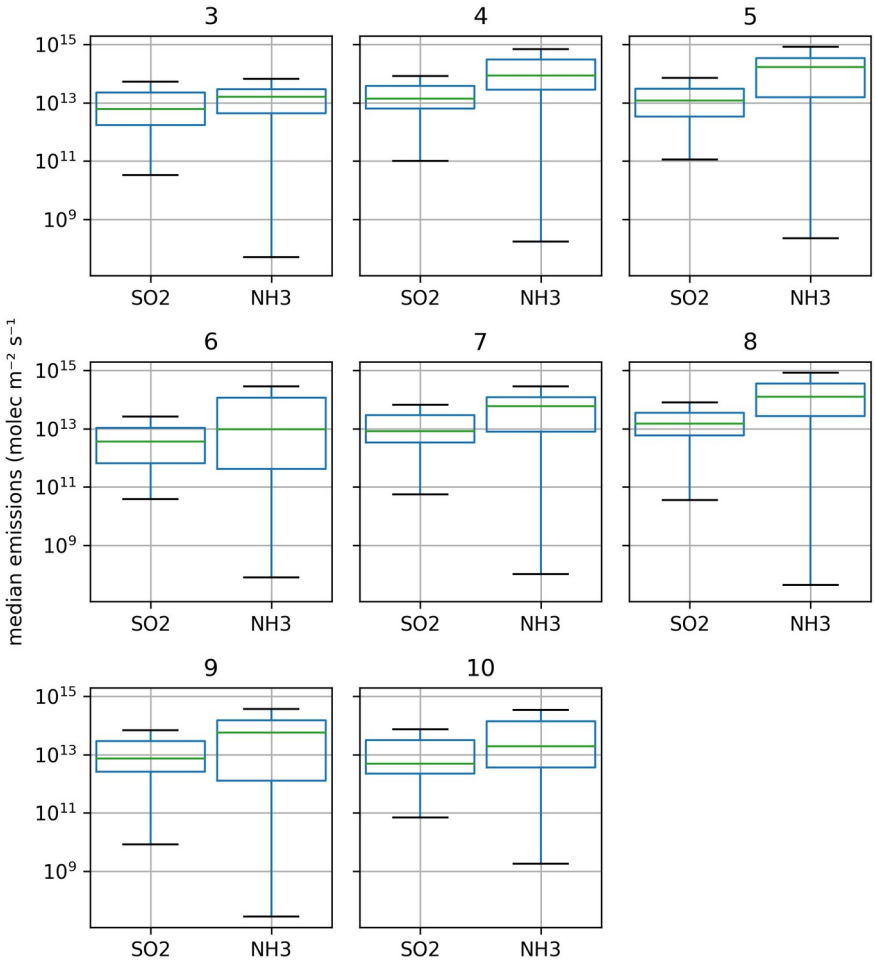

Figure S8: Median SO_2 and NH_3 emissions along trajectory (last 4 days) by month (3=Mar, 10=Oct).

Particle size distributions

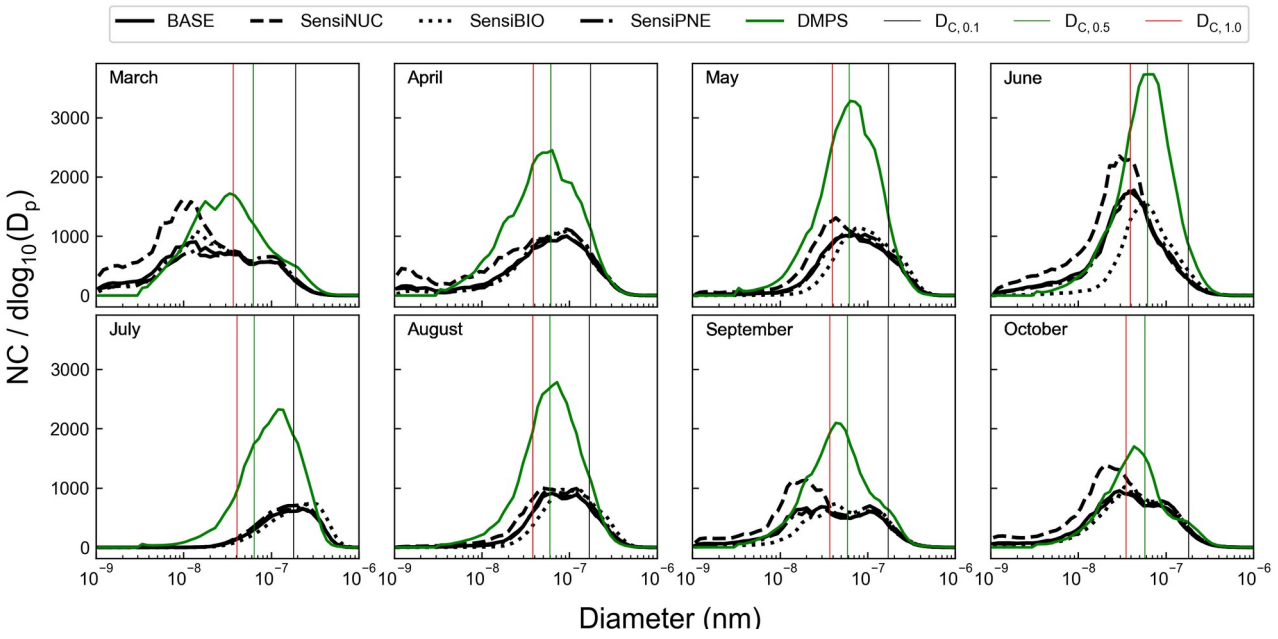

Figure 9: Median measured (DMPS) and modelled ("BASE" and "Sensi"-simulations, Table 2 in the main article) particle size distributions at the station by month for the study period. Vertical lines show the median critical dry diameters of 0.1%, 0.5% and 1.0% supersaturation.

Applied reduction in GAINS number and sea salt particle emissions

Initial simulations showed overestimation in the PM1, along with overestimation in the coarse mode number concentrations. This seemed to be due to primary number emissions (PNE and sea salt). The problem with the relatively coarse classification of the GAINS size distribution meant that mass emissions are sensitive to how the smoothing was done, as the choice of the mass mean diameter (MMD) of the uniformly distributed bins affects total mass. Furthermore, GAINS number emissions are not necessarily mass consistent. A few percent difference in the total number concentration, if applied to the largest bins, will change the total mass substantially. For these reasons, the coarse mode emissions of both sea salt and primary number emissions were multiplied with a time-invariant function that reduced the number emissions, starting from 230 nm diameter with 5% reduction, through 50% reduction in 330 nm diameter and finally 93% reduction in 1µm diameter particle number emissions. This resulted in approximately 2% reduction in total number emissions and approximately 55% reduction in PM1 mass emissions, varying somewhat with the emission size distribution.

How well do the responses predict changes in extreme case?

The response to CCN was calculated using a relatively small perturbation of model input and relating it to the change in the model CCN output. But how well does the response predict model response in case of large perturbation to the tested input? We defined the response as a linear function, because QP = QB[R(fI–1)+1], where we assume that R and fI both stay constant with respect to QB – acknowledging that both assumptions are idealizations of the real conditions. With these assumptions, when fI = 0, meaning that the process in question is completely removed, QP is due to contributions of other processes in the model. In this case QP = QB(1–R). We tested this prediction with the ZeroAER and ZeroNUC cases by comparing the prediction of the linear model to the actual model results in the Zero cases. It turns out that the linearity is a good approximation even in the extreme case of fI=0 for the primary particle emissions, but a bad approximation for the nucleation rates. Here we expand the linear form of R by noticing that the both terms in the right hand side rational function in Eq. (6) are linear approximations of the logarithm. This implies that the output factor fQ in the model is the input factor fI to the power of the response R:

$$R_{POW} = \frac{\ln(f_Q)}{\ln(f_I)} \rightarrow f_Q = f_I^{R_{POW}} = Q_P = Q_B f_I^{R_{POW}} \quad (6)$$

The problem with this model is that $f_Q \rightarrow 0$ when $f_I \rightarrow 0$, in effect neglecting other processes that contribute to the CCN NC, so we expand the equation to

$$Q_P = (Q_0 + Q_{NUC}) f_I^{R_{POW}} = Q_0 + Q_{NUC} f_I^{R_{POW}} \quad (7)$$

Where we define Q_0 as the part of Q_B for which R=0, meaning it is invariant to the process that is varied. Here the invariant part Q_0 is what the ZeroNUC solves. If we equate $CCN_{ZeroNUC}$ with Eq. (6), we can estimate the largest f_I which approximates $CCN_{ZeroNUC}$ (by minimizing the model bias, for example). We found that in CCN supersaturation classes 0.1–0.2% reducing the nucleation rates by a factor of 100, the effect of nucleation to was in practice completely removed (B_{NMBF} < 1%). In smaller CCN sizes, the nucleation rates would have to be reduced by a factor of 10^{-4}. Figure S10 shows the prediction of CCN number concentrations made with the linear function in case of primary particle emissions and nucleation, and in addition power law function in case of nucleation (using a constant f_I=10^{-3}). The linear function fails completely to predict the effect of reduced nucleation, but fairs much better with the primary emissions. For consistency, Figure S10 also shows the f_I which would minimize the bias in the power law model in the PNE cases. These factors were unrealistically high, at least 0.1, but the simpler linear model gave adequate predictions with the actual f_I=0. In all cases, the response was a useful metric to estimate the number concentrations even in the extreme case of turning off the process altogether. Figure S11 shows the same data in a time series, with red (blue) shading showing over(under)estimation by the respective model when compared with the Zero cases.

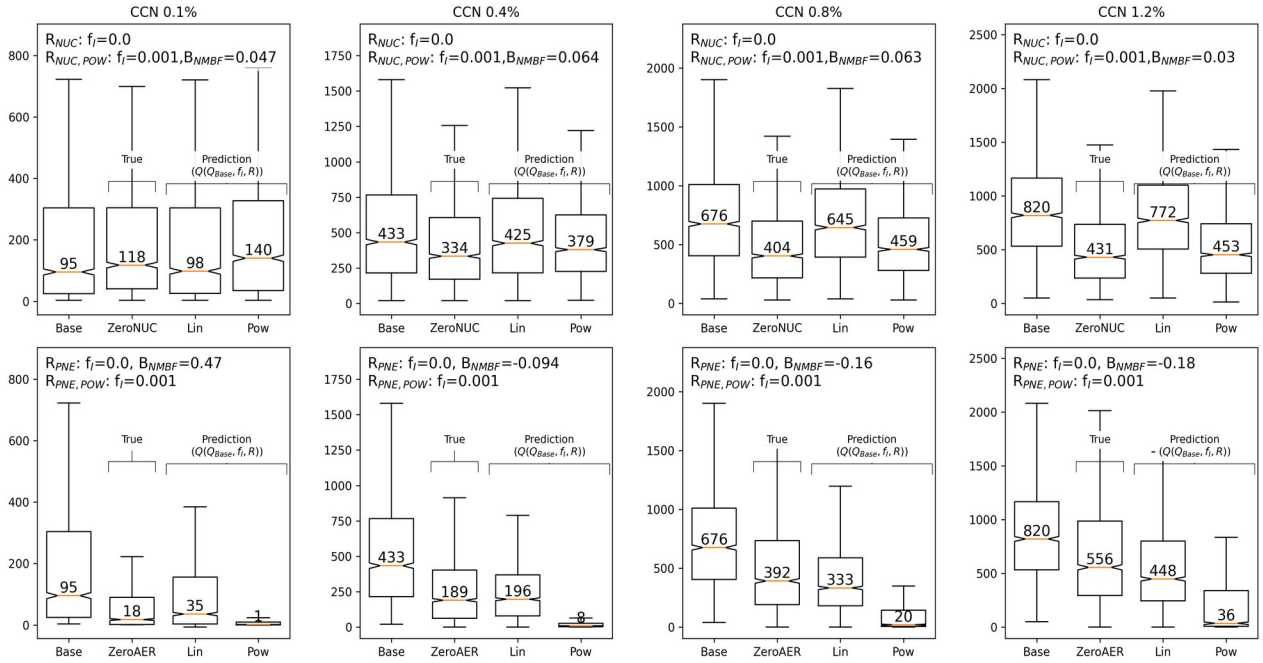

Figure S10: Boxplots of the CCN number concentrations of 0.2%, 0.4% and 1.0% supersaturation classes from the Base and Zero simulations (3-hourly, 8-months times series), and the prediction of CCN in a case where NUC or PNE would be turned off (f_l=0.0, Lin), or multiplied with a factor f_l=0.001 (Pow). Predictions were obtained by using the Base concentrations, CCN responses and the multiplication factor f_l. The B_{NMBF} of the Pow and Lin predictions is shown for NUC and PNE, respectively.

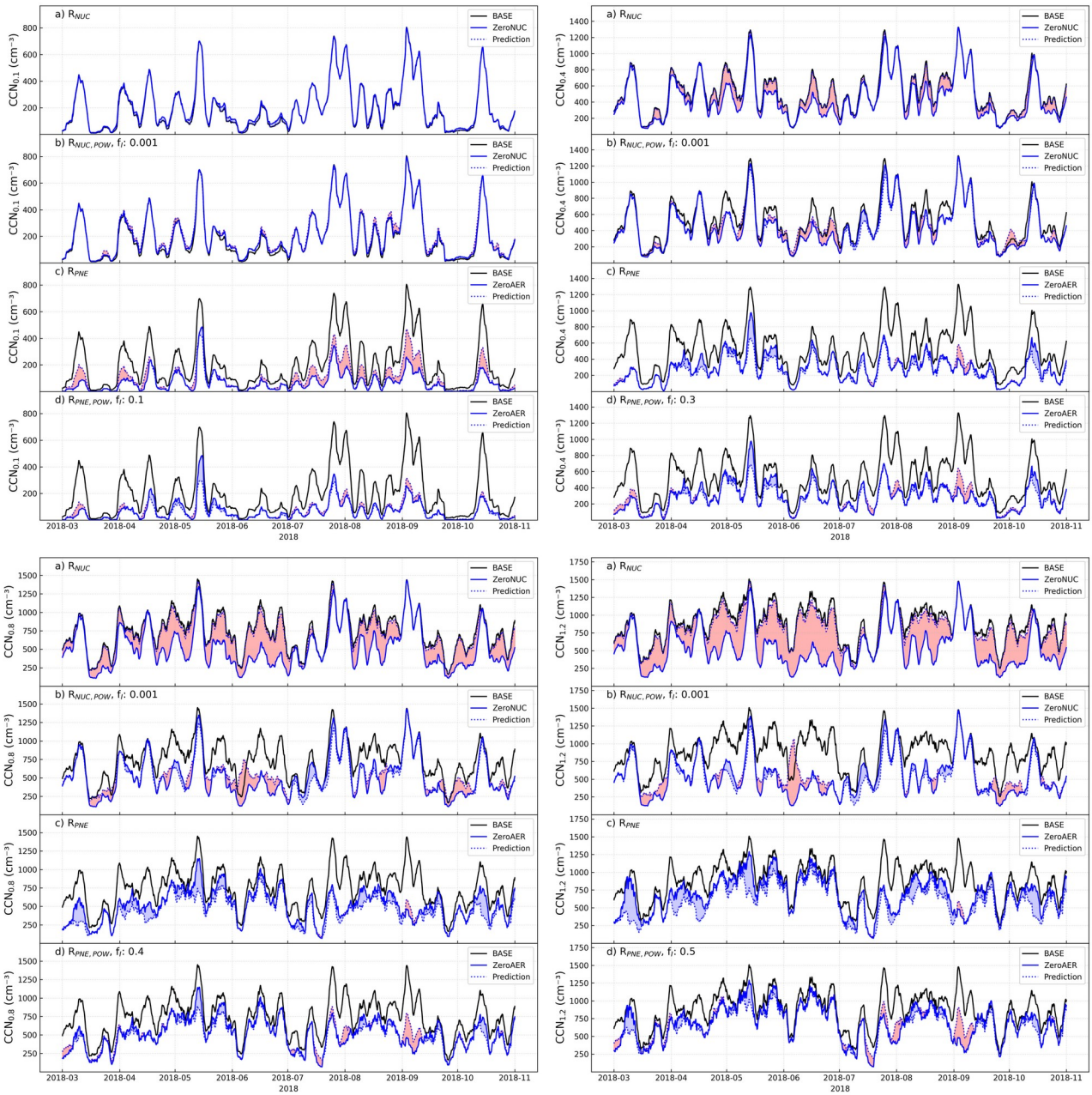

Figure S11: Time series of the CCN number concentrations of 0.2%, 0.4% and 1.0% supersaturation classes from the Base and Zero simulations (3-hourly, 8-months times series), and the prediction of CCN in a case where NUC or PNE would be turned off (fI=0.0, Lin), or multiplied with a factor fI=0.001 (Nuc,Pow). RPNE,POW uses a multiplication factor that minimizes the bias.

In conclusion, the responses calculated with perturbing the model can be used to estimate the overall contribution of the tested process. The primary emissions seem to follow the linear model better, whereas the effect of the nucleation rate is better described with the power law model. If this behaviour also holds with significantly increased nucleation rates, the low responses which appear in the exponent, mean that the CCN number concentration is rather insensitive to changes in the formation rates, at least to anything less than a magnitude. This does not imply that nucleation is unimportant, as the responses are reflecting the overall state of the system and the impact of other, possibly dominating processes. This is evident in the 8-month time series of the size distribution surface plots which shows the ZeroNUC and ZeroPNE cases; without the suppression of primary emissions, new particle formation is still able to capture general form of the observed size distribution, but with some underestimation of the accumulation mode (Figure S13). To estimate the

suppressing effect of the combined NUC and PNE to the CCN concentrations, we compare the summed CCN from the Zero-simulations against BASE ($MD(\frac{\sum [CCN]_{ZERO}}{[CCN]_{BASE}})$). For supersaturation classes 0.2%–1.2% the median ZeroNUC+ZeroPNE concentrations were ca. 28% above BASE, while the median of summed [$CCN_{0.1\%}$] was ca. 45% higher than BASE. These findings are consistent with the sensitivity studies which showed the negative impact of cluster formation rates to [$CCN_{0.1\%}$].

We calculated projections of the average impact of new particle formation, or specifically the nucleation rates, and primary number emissions to CCN, for a range of scenarios where the processes change by a factor (Figure S12). This reflects the sensitivity simulations well; while increasing nucleation rates will produce a lot more particles in the nucleation mode, this effect gets faded when considering the larger particle sizes where the CCN is found. The effect of new particle formation is dependent on the growth of the particles, and this is dependent on the condensation of organic and inorganic compounds. Figure S12 also includes the projections for the change of CCN with respect to biogenic emissions (both the linear and exponential response is shown). Naturally, these projections are simplistic in the sense that parameters are scaled uniformly, meaning all BVOC and all PNE sizes are scaled with the same factor. In real scenarios, such changes would affect the shape of the size distributions and not only the overall fluxes, similarly changes in the chemical distribution of the biogenic emissions could change the response.

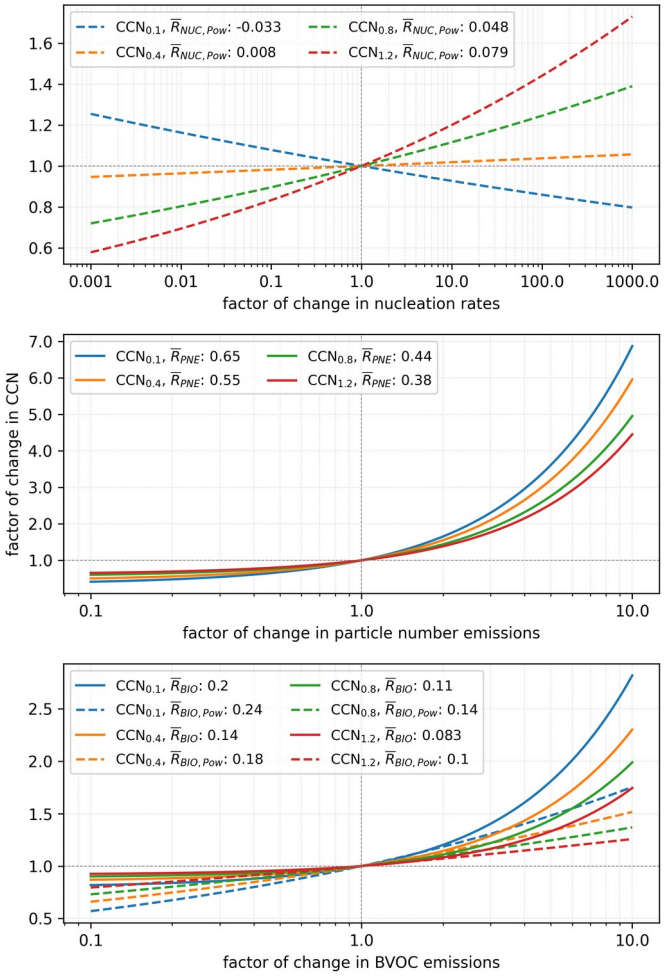

Figure S12: Projections of change in CCN as a response to change in nucleation rates, primary number and BVOC emissions, based on the calculated responses from the sensitivity runs. Note the different scales in the axes of the three panels.

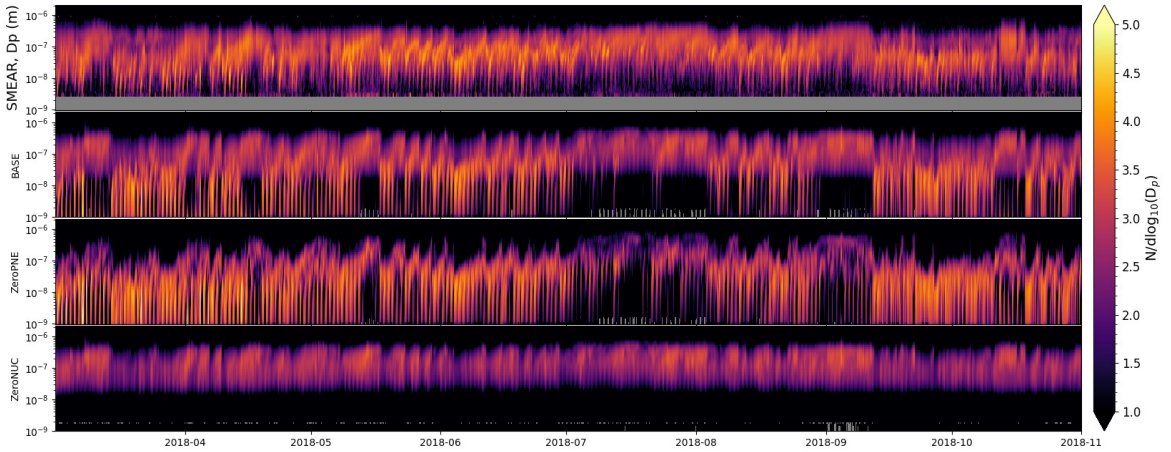

130 *Figure S13: Measured (DMPS) and modelled particle number size distributions from the BASE, ZeroPNE and ZeroNUC simulations.*

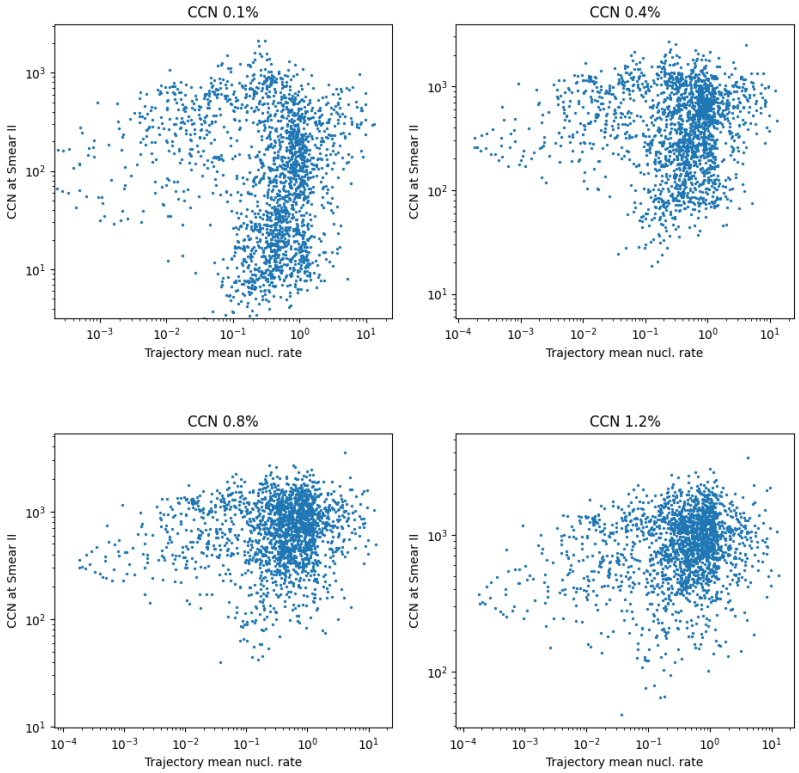

Figure S14: Scatter plot of modelled CCN at SMEAR II and mean cluster formation rate along the trajectories (0–4 days prior to SMEAR II).

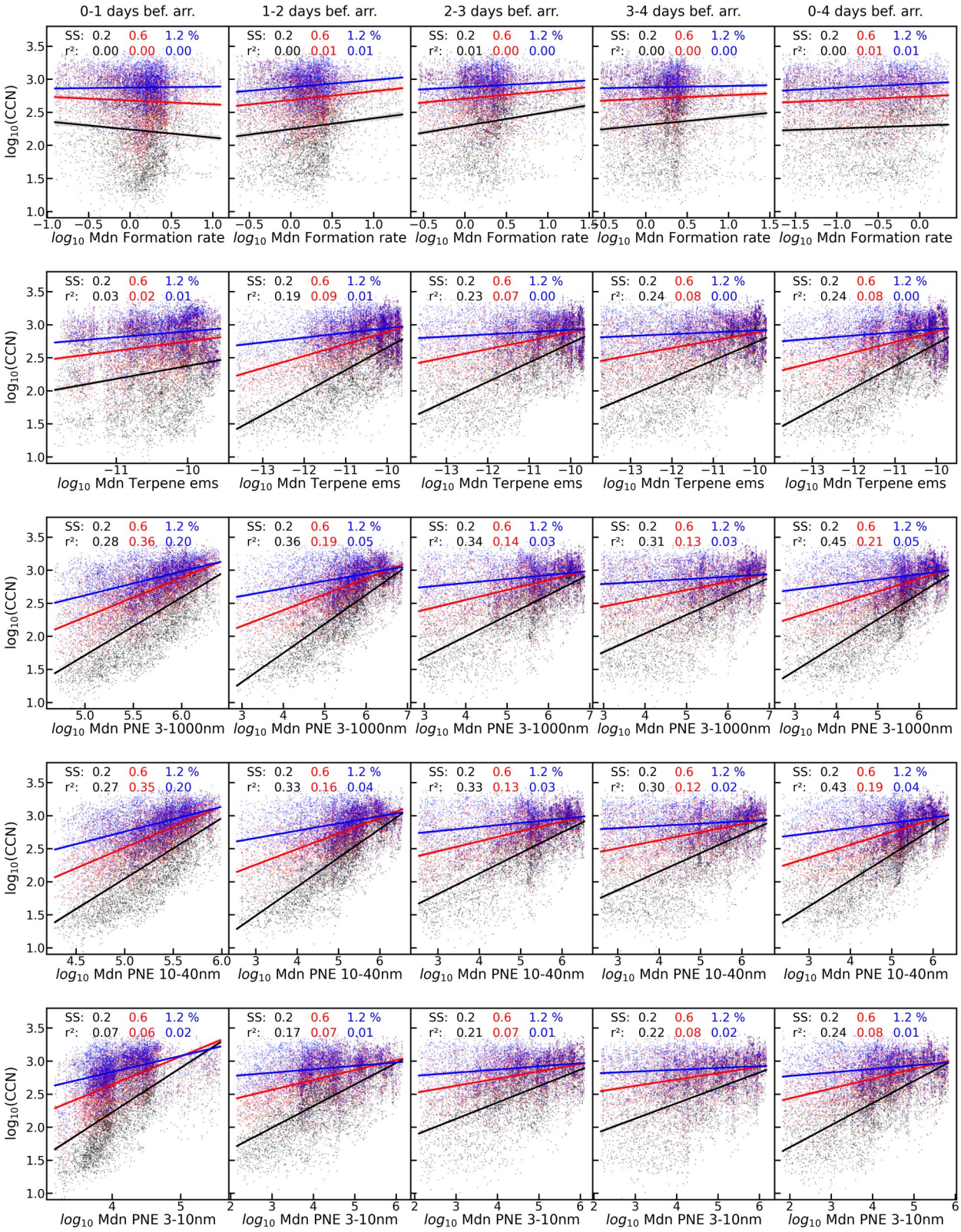

Figure S15: Scatter plots of modelled CCN at the station and various model parameters, correlating CCN at the station and the history of the parameter state along trajectories. Columns show median values of emissions and cluster formation rates 0–1, 1–2, 2–3 and 3–4 days before the trajectory arrives at the station.

Table S4: Relative change in modelled median of CCN number concentration in the two Zero-runs compared with BASE, one where primary anthropogenic particle emissions were turned off, and one where cluster formation (nucleation) was turned off. The 95% confidence intervals are calculated by bootstrapping with 50000 samplings. This table corresponds to data in Figs. 12 and 13 in the main article.

CCN	All months		Spring		Summer		Autumn	
Primary particle emissions set to zero (ZeroPNE)								
0.1%	–82%	(–86,–78)%	–87%	(–91,–83)%	–76%	(–80,–71)%	–89%	(–96,–80)%
0.4%	–56%	(–60,–53)%	–59%	(–67,–54)%	–47%	(–53–42)%	–60%	(–64,–55)%
0.8%	–42%	(–45,–38)%	–42%	(–47,–37)%	–37%	(–42,–33)%	–48%	(–53,–42)%
1.2%	–33%	(–36,–29)%	–32%	(–38,–26)%	–32%	(–38,–26)%	–35%	(–40,–28)%
Cluster formation set to zero (ZeroNUC)								
0.1%	+23%	(+12,+35)%	+35%	(+13,+58)%	+14%	(+2,+33)%	+36%	(+16,+70)%
0.4%	–22%	(–27,–18)%	–20%	(–29,–14)%	–21%	(–29,–16)%	–25%	(–35,–17)%
0.8%	–40%	(–43,–37)%	–35%	(–40,–29)%	–41%	(–45,–38)%	–43%	(–49,–38)%
1.2%	–48%	(–50,-45)%	–42%	(–47,–36)%	–50%	(–53,–47)%	–50%	(–55,–45)%

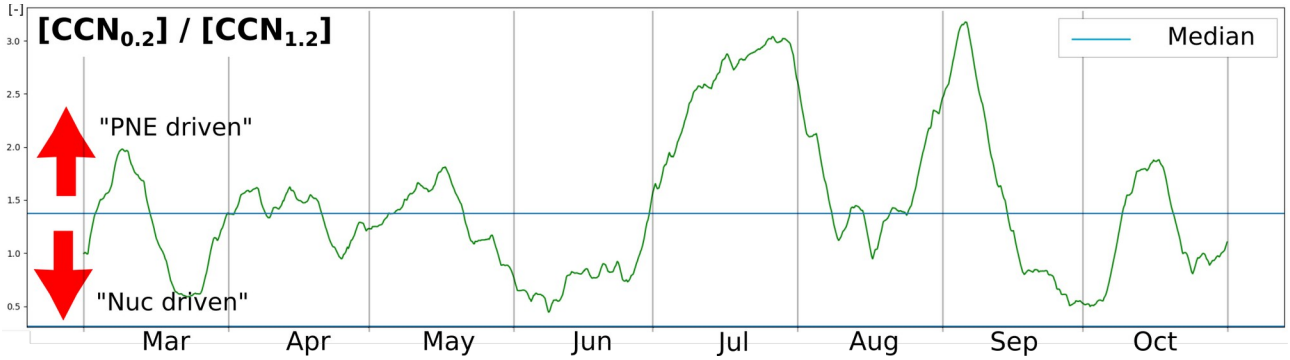

Figure 16: Ratios of $CCN_{0.2}/CCN_{1.2}$.

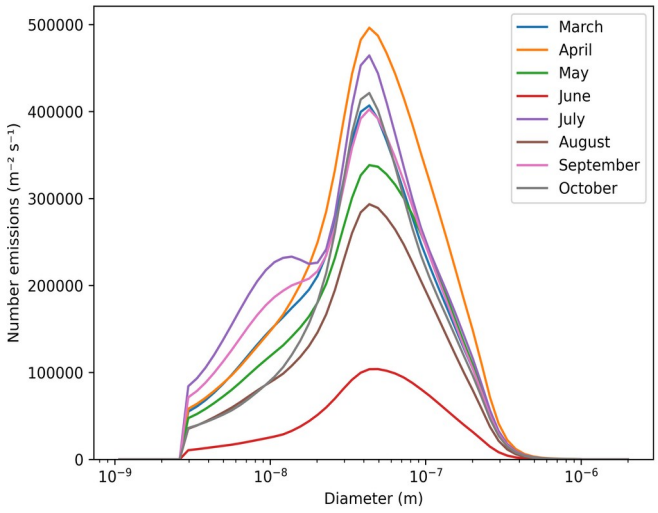

Figure S17: Mean size distributions particle number emissions along the trajectories by month.

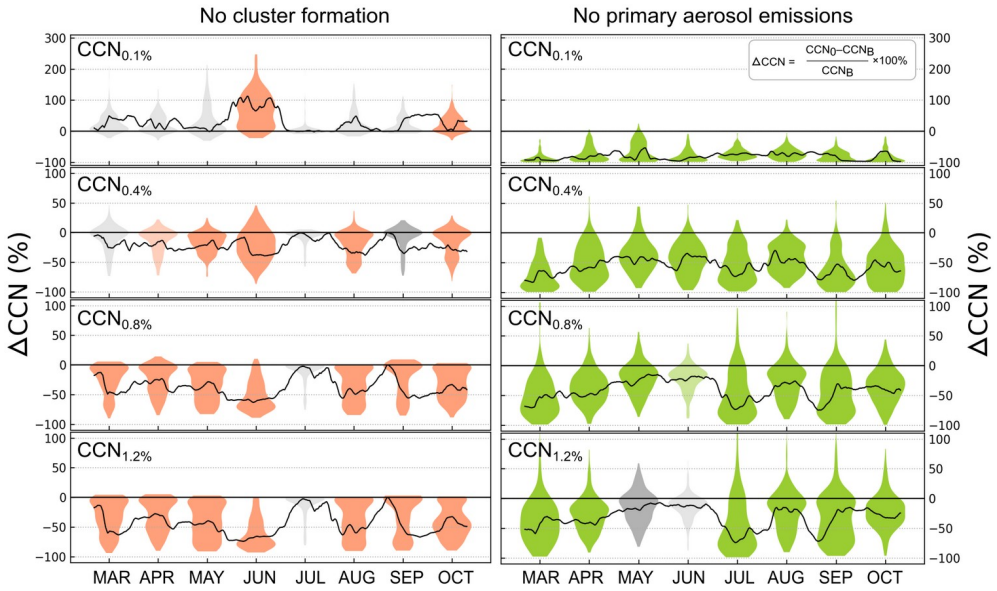

145

Figure S18: Distributions of the monthly relative changes in CCN concentrations in two model runs ZeroNUC (left panel) and ZeroPNE (right panel), aggregated from the 3-hourly modelled CCN concentration at the end of the trajectory. Coloured distributions have p-value<0.01 in the Mood's median test, while light coloured data has 0.01<p≤0.05. For gray and light gray distributions 0.1≥p>0.05 and p>0.1, respectively. The black line shows the 12-day running median of the relative difference in CCN concentrations between Zero-simulations and BASE. This figure corresponds to data in Table S4.

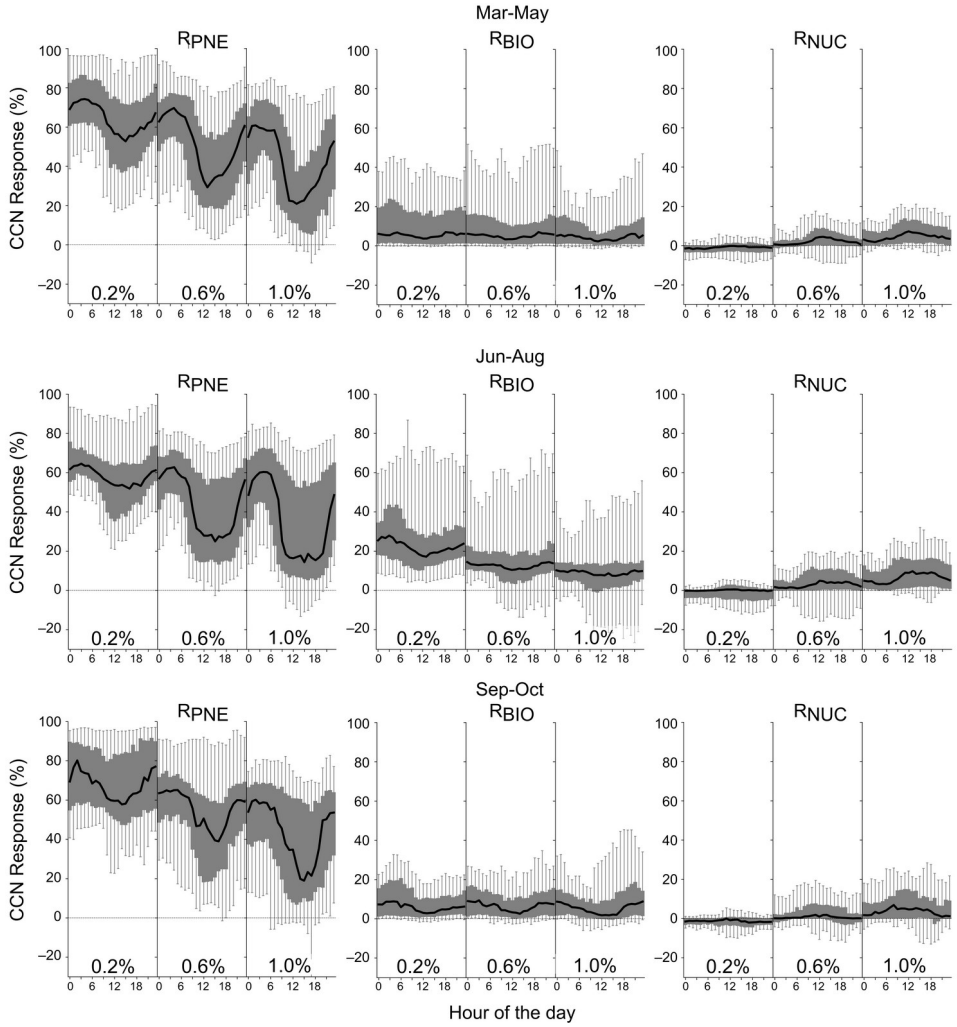

Figure S19: Diurnal profiles of the CCN responses to changes in anthropogenic particle emissions (left column), BVOC emissions (middle column) and cluster formation rate (right column) at 0.2%, 0.6% and 1.0% supersaturations during spring (top row), summer (middle row) and autumn (bottom row).

Figure S20 shows the geographical origins of the air masses as azimuths and straight line distance from the SMEAR II station for the last four days before arriving at the station, as well as some relevant model variables for CCN formation. For discussion, panel b also shows the modelled [$CCN_{0.2\%}$] and [$CCN_{1.0\%}$]. This overall view on the study period serves as a basis when we try to identify the origins (both geographical and processes) that lead to CCN. In March, cluster formation rates were average throughout the period, with low BVOC emissions. Early March peak in CCN is accompanied with some BVOC and notable PNE and cluster formation, origins from south-east, whereas second half of March saw below average CCN, PNE and BVOC, with average cluster formation, and origins from north-westerly direction. With increasing temperatures in April the BVOC emissions pick up, cluster formation is strong, but the peaks in CCN coincide more with elevated PNE (and BVOC). The end of April shows airmasses originating from west of SMEAR II, elevated cluster formation rates 3–4 days prior to station, followed by increasing BVOC emissions and decreasing particle emissions during the last two days. The resulting increase in [$CCN_{1.0\%}$] at the end of April could be a typical pathway from new particle formation to CCN, whereas the peak

in mid-May, while still showing strong BVOC emissions, seems to mostly originate from PNE. Otherwise, much of the April–June period includes trajectories with westerly to north-westerly component, formation of clusters and average [$CCN_{1.0\%}$]. Especially in June primary emissions were low, cluster formation along trajectories generally lasted for days with BVOC emissions overlapping, indicating that much of the CCN was likely formed from NPF (as also indicated by the Zero-simulations). In contrast, July and early September mostly saw periods with weak cluster formation, elevated BVOC and primary particle emissions, related to south-easterly origins of the airmasses, coinciding with some of the highest CCN concentrations in the studied time period. The different pathways of CCN origins are also supported by the fractions of [$CCN_{0.2\%}$]/[$CCN_{1.2\%}$] (Fig. S16), where low fractions are seen in end of March, end of April, June, mid-August and late September and early October, coinciding with low PNE (and lower than average fraction of 3–30 nm emissions) and suggesting formation of CCN via NPF.

Figure S21 shows the geographical origins of the airmasses in the summer (June–August), illustrated with the density of the FLEXPART Source-Receptor Relationship (SRR) values, grouped in sectors where each sector is 1000 km further away from the SMEAR II station. For clarity, the first 200 km radius is left out as the direction of advection at the station is not relevant in this context. The trajectories were divided in two groups, where the top (bottom) row is an aggregation of the trajectories that showed above (below) median CCN 0.4 %. For the most part the above median CCN trajectories showed high SOA and primary particle mass. The below median trajectories show the typical origins that favor NPF events, while the above median trajectories have a southerly component, favouring BVOC but also anthropogenic emissions, although 3–4 days prior to station the airmasses are quite dispersed and also show some NPF favoured North-Westerly component.

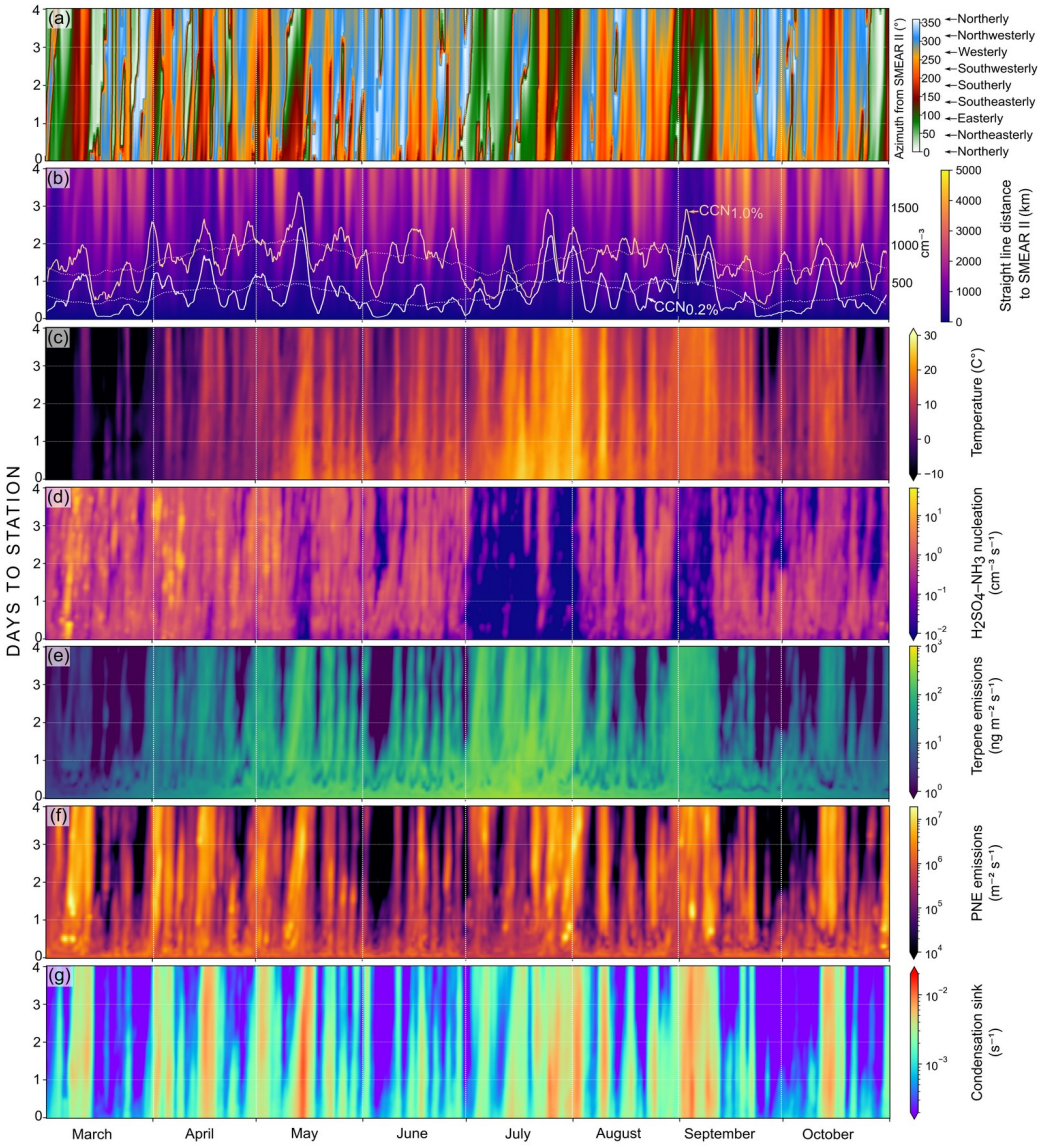

Figure S20: Hovmöller diagrams showing the 4-day history of the air masses and model parameters which are relevant to CCN formation. a) azimuth, i.e. bearing from SMEAR II; b) straight line distance (km) from the station to the trajectory mean, superimposed are the 30-day and 3-day running mean of modelled [$CCN_{0.2\%}$] and [$CCN_{1.0\%}$] at the station (right axis); c) temperatures (C°), note that the color scale only covers the range between –10°C and 30°C; d) formation rates from the ACDC H_2SO_4–NH_3 module; e) terpene (mono and sesquiterpenes) emissions; f) total primary anthropogenic particle number emissions; g) condensation sink of sulfuric acid, used as a scaling factor to estimate coagulation losses of interstitial molecular clusters in the ACDC module. 1-hour resolution data is filtered with a 12-hour gaussian kernel on the horizontal, and unfiltered on the vertical dimension.

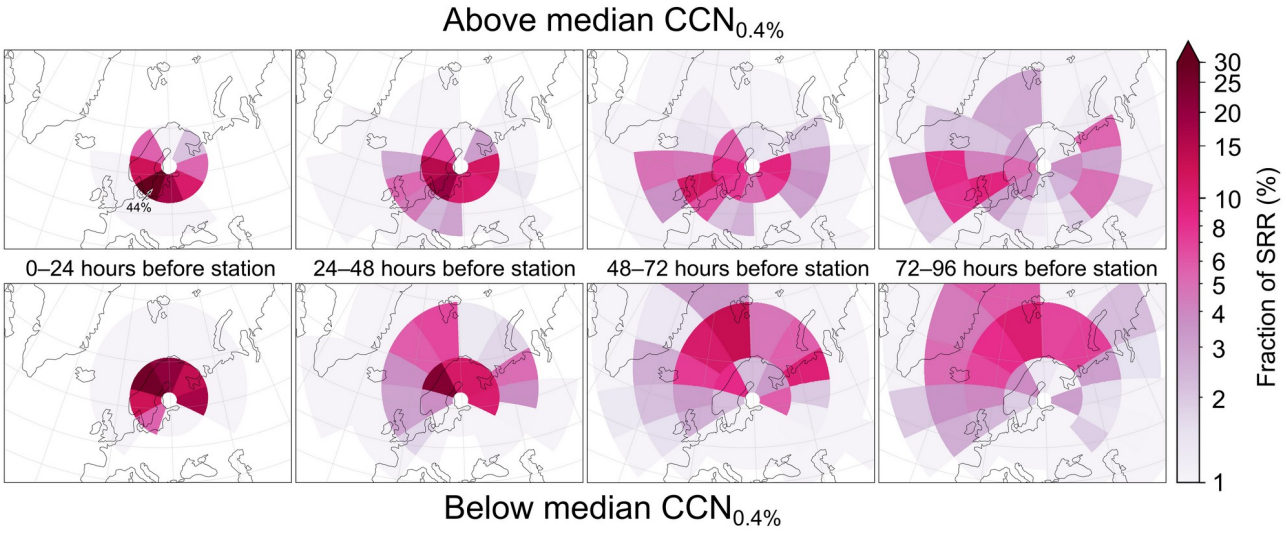

Figure S21: Locations of summertime (JJA) airmasses 0–4 days prior to arriving at the SMEAR II, based on the FLEXPART Source-Receptor Relationship (SRR) distribution. The aggregated SRR data were divided by the modelled [$CCN_{0.4\%}$] so that top row shows trajectories which showed more than JJA median, and bottom row trajectories whose [CCN] was below JJA median. The radial distance of each sector edge is 1000 km further from the previous (the traces within innermost 200 km radius from SMEAR II station were omitted from the calculation). Note that the colour scaling is logarithmic (fraction is shown on the map if it exceeds the scale).

References

Caffrey, P. F., Ondov, J. M., Zufall, M. J. and Davidson, C. I.: Determination of Size-Dependent Dry Particle Deposition Velocities with Multiple Intrinsic Elemental Tracers, Environmental Science & Technology, 32, 1615-1622, 10.1021/es970644f, 1998.

Farmer, D. K., Boedicker, E. K. and DeBolt, H. M.: Dry Deposition of Atmospheric Aerosols: Approaches, Observations, and Mechanisms, Ann. Phys. Chem., 72, 375-397, 10.1146/annurev-physchem-090519-034936, 2021.

Gallagher, M., Beswick, K., Duyzer, J., Westrate, H., Choularton, T. and Hummelshøj, P.: Measurements of aerosol fluxes to speulder forest using a micrometeorological technique, Atmos. Environ., 31, 359-373, 10.1016/s1352-2310(96)00057-x, 1997.

Gaman, A., Rannik, U., Aalto, P., Pohja, T., Siivola, E., Kulmala, M. and Vesala, T.: Relaxed eddy accumulation system for size-resolved aerosol particle flux measurements, J. Atmos. Ocean. Tech., 21, 933-943, 2004.

Gordon, M., Staebler, R. M., Liggio, J., Vlasenko, A., Li, S.-M. and Hayden, K.: Aerosol flux measurements above a mixed forest at Borden, Ontario, Atmos. Chem. Phys., 11, 6773-6786, 10.5194/acp-11-6773-2011, 2011.

Groenholm, T., Launiainen, S., Ahlm, L., Martensson, E. M.., Kulmala, M., Vesala, T. and Nilsson, E. D..: Aerosol particle dry deposition to canopy and forest floor measured by two-layer eddy covariance system, Journal of Geophysical Research: Atmospheres, 114, D04202, 10.1029/2008JD010663, 2009.

Grönholm, T., Aalto, P. P., Hiltunen, V., Rannik, Ü., Rinne, J., Laakso, L., Hyvönen, S., Vesala, T. and Kulmala, M.: Measurements of aerosol particle dry deposition velocity using the relaxed eddy accumulation technique, Tellus B., 59, 10.3402/tellusb.v59i3.16998, 2007.

Grosch, S. & Schmitt, G.: Experimental Investigations on the Deposition of Trace Elements in Forest Areas, in: Environmental Meteorology, Springer Netherlands, 201-216, 10.1007/978-94-009-2939-5_15, 1988.

Höfken, K. D. & Gravenhorst, G.: Deposition of Atmospheric Aerosol Particles to Beech- and Spruce Forest, in: Deposition of Atmospheric Pollutants, edited by: , Springer Netherlands, 191-194, 10.1007/978-94-009-7864-5_19, 1982.

Lavi, A., Farmer, D. K., Segre, E., Moise, T., Rotenberg, E., Jimenez, J. L. and Rudich, Y.: Fluxes of Fine Particles Over a Semi-Arid Pine Forest: Possible Effects of a Complex Terrain, Aerosol Sci. Technol., 47, 906-915, 10.1080/02786826.2013.800940, 2013.

Lorenz, R. and Murphy, C. E.: Dry deposition of particles to a pine plantation, Boundary Layer Meteorol., 46, 355-366, 10.1007/bf00172241, 1989.

Mammarella, I., Rannik, U., Aalto, P., Keronen, P., Vesala, T. and Kulmala, M.: Long-term aerosol particle flux observations. Part II: Particle size statistics and deposition velocities, Atmos. Environ., 45, 3794-3805, 10.1016/j.atmosenv.2011.04.022, 2011.

Möller, U. and Schumann, G.: Mechanisms of transport from the atmosphere to the Earth's surface, J. Geophys. Res., 75, 3013-3019, 10.1029/jc075i015p03013, 1970.

Paramonov, M., Aalto, P. P., Asmi, A., Prisle, N., Kerminen, V.-M., Kulmala, M. and Petäjä, T.: The analysis of size-segregated cloud condensation nuclei counter (CCNC) data and its implications for cloud droplet activation, Atmos. Chem. Phys., 13, 10285-10301, 10.5194/acp-13-10285-2013, 2013.

Petters, M. D. and Kreidenweis, S. M.: A single parameter representation of hygroscopic growth and cloud condensation nucleus activity, Atmos. Chem. Phys., 7, 1961-1971, 10.5194/acp-7-1961-2007, 2007.

Pryor, S.: Size-resolved particle deposition velocities of sub-100 nm diameter particles over a forest, Atmos. Environ., 40, 6192–200, 2006.

Pryor, S. C., Barthelmie, R. J., Spaulding, A. M., Larsen, S. E. and Petroff, A.: Size-resolved fluxes of sub-100-nm particles over forests, Journal of Geophysical Research: Atmospheres, 114, 10.1029/2009jd012248, 2009.

Pryor, S. C., Gallagher, M., Sievering, H., Larsen, S. E., Barthelmie, R. J., Birsan, F., Nemitz, E., Rinne, J., Kulmala, M., Grönholm, T., Taipale, R. and Vesala, T.: A review of measurement and modelling results of particle atmosphere–surface exchange, Tellus B: Chemical and Physical Meteorology, 60, 42, 10.1111/j.1600-0889.2007.00298.x, 2008.

Qi, J., Yu, Y., Yao, X., Gang, Y. and Gao, H.: Dry deposition fluxes of inorganic nitrogen and phosphorus in atmospheric aerosols over the Marginal Seas and Northwest Pacific, Atmos. Res., 245, 105076, 10.1016/j.atmosres.2020.105076, 2020.

Sehmel, G.: Particle eddy diffusivities and deposition velocities for isothermal flow and smooth surfaces, J. Aerosol Sci., 4(2), 125–38, 1973.

Simpson, D., Benedictow, A., Berge, H., Bergström, R., Emberson, L. D., Fagerli, H., Flechard, C. R., Hayman, G. D., Gauss, M., Jonson, J. E., Jenkin, M. E., Nyíri, A., Richter, C., Semeena, V. S., Tsyro, S., Tuovinen, J.-P., Valdebenito, Á. and Wind, P.: The EMEP MSC-W chemical transport model – technical description, Atmos. Chem. Phys., 12, 7825-7865, 10.5194/acp-12-7825-2012, 2012.

Vong, R. J., Vong, I. J., Vickers, D. and Covert, D. S.: Size-dependent aerosol deposition velocities during BEARPEX'07, Atmos. Chem. Phys., 10, 5749-5758, 10.5194/acp-10-5749-2010, 2010.

Waraghai, A. & Gravenhorst, G.: Dry Deposition of Atmoshperic Particles to an Old Spruce Stand, in: Mechanisms and Effects of Pollutant-Transfer into Forests, edited by: , Springer Netherlands, 77-86, 10.1007/978-94-009-1023-2_9, 1989.

Yu, S., Eder, B., Dennis, R., Chu, S. and Schwartz, S. E.: New unbiased symmetric metrics for evaluation of air quality models, Atmos. Sci. Lett., 7, 26-34, 10.1002/asl.125, 2006.

Zhang, X., Cappa, C. D., Jathar, S. H., McVay, R. C., Ensberg, J. J., Kleeman, M. J. and Seinfeld, J. H.: Influence of vapor wall loss in laboratory chambers on yields of secondary organic aerosol, Proc. Natl. Acad. Sci., 111, 5802–5807, https://doi.org/10.1073/pnas.1404727111, 2014.

Zufall, M., Davidson, C., Caffrey, P. and Ondov, J.: Airborne concentrations and dry deposition fluxes of particulate species to surrogate surfaces deployed in southern Lake Michigan., Environ. Sci. Technol., 32, 1623–28, 1998.